Wave propagation and instabilities in monolithic and periodically structured elastomeric materials undergoing large deformations

K. Bertoldi[1,2] and M. C. Boyce[1]

[1]*Department of Mechanical Engineering, Massachusetts Institute of Technology, Cambridge, Massachusetts 02139-4307, USA*
[2]*Multi Scale Mechanics (MSM), TS, CTW, Universiteit Twente, P.O. Box 217, 7500 AE Enschede, Netherlands*

Wave propagation in elastomeric materials undergoing large deformations is relevant in numerous application areas, including nondestructive testing of materials and ultrasound techniques, where finite deformations and corresponding stress states can influence wave propagation and hence interpretation of data. In the case of periodically structured hyperelastic solids, the effect of deformation on the propagation of acoustic waves can be even more dramatic. In fact, transformations in the periodic patterns have been observed upon application of load due to microstructural elastic instabilities, providing opportunities for transformative phononic crystals which can switch band-gap structure in a sudden, but controlled manner. Here both analytical and numerical techniques are presented for assessing the influence of finite deformations on the propagation of elastic waves in both monolithic as well as periodically structured elastomeric materials. Both elastic instabilities and propagation of acoustic waves are strongly influenced by geometric pattern, material properties and loading conditions, giving different opportunities for tuning and manipulating the location and presence of instabilities and phononic band gaps.

PACS number(s): 62.30.+d, 43.40.+s, 46.40.Cd

I. INTRODUCTION

The problem of elastic wave propagation through predeformed nonlinear elastic materials is of interest in numerous application areas. Nondestructive testing of materials involves sending waves through structures, which are often prestressed during an assembly or curing process. Modeling wave propagation in biological materials is important in ultrasound techniques and biological soft tissues are often in a prestressed state due to growth and remodeling.

Hence the study of the propagation of elastic waves through prestressed structures is of great importance with specific interest in determining the effects of finite deformation on the response of the structure. Clearly, large prestresses induce privileged directions inside the deformed material, whose influence on the wave speed may not be negligible. The analysis of incremental (infinitesimal) motions superimposed onto a large predeformation provides a natural framework to address this problem. However, analysis of these physics requires sophisticated calculations which account for the effects of the nonlinear deformation (including nonlinear material behavior, nonlinear geometry effects which accompany finite deformations, and inhomogeneous stress fields which develop with deformation) on the propagation of elastic waves.

Structural materials are often inhomogeneous on small scales and possess specific microstructure. An example is given by cellular solids, whose connection between microstructure and mechanical properties has been intensely investigated.[1] The use of periodic structures as phononic crystals (e.g., periodic solids with a range in frequency where elastic wave propagation is barred) has been of growing interest in recent years due to their potential as sound filters, acoustic mirrors, acoustic wave guides, vibration isolators and in transducer design. Many solid-solid, solid-fluid, and solid-air structures have been pursued through experiments and/or simulation.[2–14] Moreover studies have focused on the sound-light interplay in periodic systems.[15–17] Recently solids with periodicity at the sub-micron scale have attracted increasing attention. Their applications include photonic and phononic band-gap materials, filtration, microfluidic networks, porous biomaterials as tissue engineering scaffolds with tunable biocompatible and biodegradable properties, and DNA/protein microarrays.[18–22]

The structural integrity of periodic structures under various external stimuli is a critical issue which is frequently overlooked. In fact, when these structures are subjected to external stress their periodic geometry can suddenly change at a critical point due to mechanical instability of the structural elements leading to dramatic pattern transformation. Buckling instabilities responsible for these transformations are ubiquitous phenomena observed at all length scales in a wide range of materials in both natural and man-made systems. While the physical phenomenon has been known for a long time, its utilization from a technological standpoint is recent. Mechanical instabilities have been exploited to assemble complex patterns,[23,24] to fabricate stretchable electronics[25] and microlens arrays[26] and as a novel metrology technique for elastic modulus of ultrathin polymeric films.[27]

Recently, reversible pattern transformation in square and oblique arrays of circular holes in a neo-Hookean matrix (at the millimeter scale) subjected to an external load has been uncovered[28,29] and the ability to use the pattern switch to transform their phononic band gaps has been demonstrated.[30] Since the pattern switch is the result of an elastic instability, it is both repeatable and reversible, providing opportunities for transformative phononic crystals which can switch in a sudden, but controlled manner.

Here a systematic formulation allowing the study of both instabilities (Secs. II A 1 and II A 2) and wave propagation (Secs. II 1 and II A 3) in infinite monolithic and periodic structures is presented. Then, in Sec. III the effects of geometry, material properties, loading conditions and fillers on

both elastic instabilities and propagation of acoustic waves are investigated.

II. GOVERNING EQUATIONS

Let us consider a material particle **X** that is deformed to **x** through a motion

$$\mathbf{x} = \boldsymbol{\chi}(\mathbf{X}, t), \tag{1}$$

so that the deformation gradient is defined as

$$\mathbf{F} = \frac{\partial \mathbf{x}}{\partial \mathbf{X}}. \tag{2}$$

In the undeformed configuration, the equations of motion in the absence of body forces are given by

$$\text{Div } \mathbf{S} = \rho_0 \frac{D^2 \boldsymbol{\chi}}{Dt^2}, \tag{3}$$

where **S** denotes the first Piola-Kirchhoff stress tensor, ρ_0 the density in the reference configuration, and D/Dt the material time derivative. If the body is at rest $D\boldsymbol{\chi}/Dt = 0$ everywhere, Eq. (3) reduces to the static equilibrium equation

$$\text{Div } \mathbf{S} = 0. \tag{4}$$

Here, we consider a body composed of a homogeneous and isotropic hyperelastic material with strain energy density W dependent on the invariants of the right Cauchy-Green tensor $\mathbf{C} = \mathbf{F}^T \mathbf{F}$ (or, alternatively, also the left Cauchy-Green tensor $\mathbf{B} = \mathbf{F}\mathbf{F}^T$),

$$W = W(I_1, I_2, I_3), \tag{5}$$

where

$$I_1 = \text{tr}(\mathbf{C}), \quad I_2 = \frac{1}{2}[\text{tr}(\mathbf{C})^2 - \text{tr } \mathbf{C}^2], \quad I_3 = \det(\mathbf{C}). \tag{6}$$

For compressible materials, the first Piola-Kirchoff stress tensor **S** is then given by

$$\mathbf{S} = \frac{\partial W}{\partial \mathbf{F}}. \tag{7}$$

Now we consider an incremental deformation superimposed upon a given strain. Incremental displacements are given by $\dot{\mathbf{x}}(\mathbf{X}, t)$, with $(\dot{\ })$ denoting a small increment in the quantity concerned. Taking the rate form of Eq. (3), we obtain the incremental version of the equations of motion referred to the reference (undeformed) configuration

$$\text{Div } \dot{\mathbf{S}} = \rho_0 \frac{D^2 \dot{\mathbf{x}}}{Dt^2}, \tag{8}$$

where

$$\dot{\mathbf{F}} = \frac{\partial \dot{\mathbf{x}}}{\partial \mathbf{X}}, \dot{F}_{ij} = \dot{x}_{i,j}. \tag{9}$$

Similarly, the incremental version of the static equilibrium equations referred to the reference (undeformed) configuration is obtained from Eq. (4) as

$$\text{Div } \dot{\mathbf{S}} = 0. \tag{10}$$

The material incremental constitutive law can be written as

$$\dot{\mathbf{S}} = \mathbb{L}{:}\dot{\mathbf{F}}, \quad \dot{S}_{ij} = \mathbb{L}_{ijkl}\dot{F}_{kl}, \tag{11}$$

where $\mathbb{L}$ is the fourth-order incremental moduli tensor, whose components are given by

$$\mathbb{L}_{ijkl} = \frac{\partial^2 W}{\partial F_{ij} \partial F_{kl}}. \tag{12}$$

Introduction of Eq. (11) into Eqs. (8) and (10) yields

$$\mathbb{L}_{ijkl}\dot{x}_{k,lj} = \rho_0 \frac{D^2 \dot{x}_i}{Dt^2}, \tag{13}$$

and

$$\mathbb{L}_{ijkl}\dot{x}_{k,lj} = 0, \tag{14}$$

respectively.

1. Wave propagation in an infinite prestressed hyperelastic monolithic solid

Let us consider the incremental wave motion

$$\dot{\mathbf{x}}(\mathbf{X}, t) = \dot{\boldsymbol{\kappa}}(\mathbf{X})\exp[-i\omega t], \tag{15}$$

where ω is the frequency of vibration. It follows from Eq. (11) that the stress is complex valued as well,

$$\dot{\mathbf{S}} = \dot{\boldsymbol{\mathcal{S}}} \exp[-i\omega t], \tag{16}$$

so that the equations of motions [Eq. (8)] become

$$\text{Div } \dot{\boldsymbol{\mathcal{S}}} + \rho_0 \omega^2 \dot{\boldsymbol{\kappa}} = 0. \tag{17}$$

For an infinite monolithic solid the incremental displacements are given by

$$\dot{\boldsymbol{\kappa}} = \hat{\boldsymbol{\kappa}} \exp[i\mathbf{K}^0 \cdot \mathbf{X}], \tag{18}$$

$\mathbf{K}^0$ being the Bloch wave vector that defines the direction of propagation of the wave. Insertion of Eqs. (15) and (18) into Eq. (13) yields

$$\mathbb{L}_{ijkl}\hat{\kappa}_k K_j^0 K_l^0 = \rho_0 \omega^2 \hat{\kappa}_i, \tag{19}$$

or

$$\mathbf{Q}\hat{\boldsymbol{\kappa}} = \rho_0 \omega^2 \hat{\boldsymbol{\kappa}}, \tag{20}$$

Q being the acoustic tensor defined as

$$Q_{ik} = \mathbb{L}_{ijkl}K_j^0 K_l^0. \tag{21}$$

It follows from Eq. (20) that the eigenfrequencies ω of the propagating waves for a given Bloch wave vector $\mathbf{K}^0$ are obtained from the eigenvalues q_i of the acoustic tensor **Q** as

$$\omega_i = \sqrt{\frac{q_i}{\rho_0}}, \quad i = 1, 2, 3. \tag{22}$$

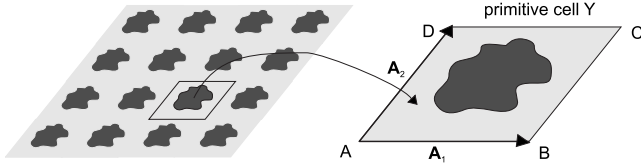Since **Q** is dependent on deformation, the eigenfrequencies ω_i will depend on deformation.

FIG. 1. Infinite periodic solid (left) and corresponding primitive cell **Y** (right).

A. Infinite hyperelastic periodically structured solid

Here, an infinite solid with a periodic microstructure in the X_1-X_2 plane is considered as depicted in Fig. 1. The solid is deformed under finite, plane strain conditions and a full Lagrangian formulation is adopted. The periodic solid is characterized by a primitive cell **Y** spanned by the lattice vectors **A**$_1$ and **A**$_2$ in the undeformed configuration.

Thus any space function ψ must satisfy the periodic conditions

$$\psi(\mathbf{X} + \mathbf{R}) = \psi(\mathbf{X}), \qquad (23)$$

where

$$\mathbf{R} = p_1 \mathbf{A}_1 + p_2 \mathbf{A}_2, \qquad (24)$$

$p = (p_1, p_2)$ being a multi-index with integer components p_i. For later use, the unit cell of the reciprocal lattice is introduced, defined by the vectors **B**$_1$ and **B**$_2$,

$$\mathbf{B}_1 = 2\pi \frac{\mathbf{A}_2 \times \mathbf{e}}{A}, \quad \mathbf{B}_2 = 2\pi \frac{\mathbf{e} \times \mathbf{A}_1}{A}, \qquad (25)$$

with $A = \|\mathbf{A}_1 \times \mathbf{A}_2\|$ and $\mathbf{e} = (\mathbf{A}_1 \times \mathbf{A}_2)/A$, so that

$$\mathbf{A}_i \cdot \mathbf{B}_j = 2\pi \delta_{ij}, \qquad (26)$$

δ_{ij} being the Kronecker delta.

1. Microscopic instability

For an infinite periodic solid an instability may occur upon application of deformation, altering the periodicity of the solid. However, the investigation of bifurcation for infinite periodic solids may still be performed on the primitive cell **Y** employing a Bloch wave analysis.[29,31,32] The analysis provides the point along the loading path where instability occurs as well as the new periodicity of the structure.

Let us consider an infinite periodic solid with a primitive cell **Y** defined by the lattice vectors **A**$_1$ and **A**$_2$ as shown in Fig. 1. Our focus is to determine when instability for the periodic solid occurs as well as the new periodicity that characterizes the structure after instability.

To investigate these circumstances, Eq. (23) is compared with the classical Bloch condition[33]

$$\psi(\mathbf{X} + \mathbf{R}) = \psi(\mathbf{X})\exp[i\mathbf{K}^0 \cdot \mathbf{R}], \qquad (27)$$

where $\mathbf{K}^0$ denotes the Bloch wave vector. It is clear that they are identical when

$$\exp[i\mathbf{K}^0 \cdot \mathbf{R}] = 1. \qquad (28)$$

Condition (28) can only be achieved when

$$\mathbf{K}^0 = K_1^0 \mathbf{B}_1 + K_2^0 \mathbf{B}_2, \qquad (29)$$

together with

$$p_i K_i^0 = 1, \quad i = 1, 2, \qquad (30)$$

B$_1$ and **B**$_2$ being the vectors defining the reciprocal lattice as defined in Eq. (25).

Thus instability occurs at the first point along the loading path for which a Bloch wave vector $\mathbf{K}^0$ exists such that an incremental displacement field $\dot{\mathbf{x}}$ different from zero everywhere exists that satisfies the incremental equilibrium equation given in Eq. (14). The instability yields an enlarged postbifurcation primitive cell characterized by $p_1 = 1/K_1^0$ and $p_2 = 1/K_2^0$ original primitive cells along the two lattice directions.

Here the finite-element method is utilized to calculate the instability for an infinite periodically structured solid subjected to a macroscopic deformation.[13,29] After construction of the mesh for the primitive cell **Y**, incremental displacements given by the Bloch type relation,

$$\dot{\boldsymbol{\kappa}}(\mathbf{X} + \mathbf{R}) = \dot{\boldsymbol{\kappa}}(\mathbf{X})\exp[i\mathbf{K}^0 \cdot \mathbf{R}], \qquad (31)$$

are applied to its external boundaries, with $\mathbf{K}^0$ defined in Eq. (29) lying in the unit cell of the reciprocal lattice, i.e., $0 \le K_1^0 < 1$ and $0 \le K_2^0 < 1$. It follows from Eq. (11) that the incremental stresses at the point where velocities (31) are applied satisfy an equivalent periodic relation,

$$\dot{\boldsymbol{\mathcal{S}}}(\mathbf{X} + \mathbf{R}) = \dot{\boldsymbol{\mathcal{S}}}(\mathbf{X})\exp[i\mathbf{K}^0 \cdot \mathbf{R}]. \qquad (32)$$

Since pairs of equivalent points on the boundary of the periodic cell **Y** have outward normal vectors in opposite directions [i.e., $\mathbf{N}(\mathbf{X}) = -\mathbf{N}(\mathbf{X}+\mathbf{R})$] the incremental traction vectors $\dot{\boldsymbol{\mathcal{T}}} = \dot{\boldsymbol{\mathcal{S}}}\mathbf{N}$ evaluated along opposite sides of the primitive cell **Y** are related through

$$\dot{\boldsymbol{\mathcal{T}}}(\mathbf{X} + \mathbf{R}) = -\dot{\boldsymbol{\mathcal{T}}}(\mathbf{X})\exp[i\mathbf{K}^0 \cdot \mathbf{R}]. \qquad (33)$$

Equations (31) and (33) imply that the incremental displacements $\dot{\mathbf{x}}$ and tractions $\dot{\mathbf{T}}$ evaluated along opposite sides of the primitive cell **Y** (Fig. 1) are related through

$$\dot{\boldsymbol{\kappa}}_{DC} = \alpha_2 \dot{\boldsymbol{\kappa}}_{AB}, \quad \dot{\boldsymbol{\mathcal{T}}}_{DC} = -\alpha_2 \dot{\boldsymbol{\mathcal{T}}}_{AB},$$

$$\dot{\boldsymbol{\kappa}}_{BC} = \alpha_1 \dot{\boldsymbol{\kappa}}_{AD}, \quad \dot{\boldsymbol{\mathcal{T}}}_{BC} = -\alpha_1 \dot{\boldsymbol{\mathcal{T}}}_{AD},$$

$$\dot{\boldsymbol{\kappa}}_B = \alpha_1 \dot{\boldsymbol{\kappa}}_A, \quad \dot{\boldsymbol{\mathcal{T}}}_B = -\alpha_1 \dot{\boldsymbol{\mathcal{T}}}_A,$$

$$\dot{\boldsymbol{\kappa}}_D = \alpha_2 \dot{\boldsymbol{\kappa}}_A, \quad \dot{\boldsymbol{\mathcal{T}}}_D = -\alpha_2 \dot{\boldsymbol{\mathcal{T}}}_A,$$

$$\dot{\boldsymbol{\kappa}}_C = \alpha_1 \alpha_2 \dot{\boldsymbol{\kappa}}_A, \quad \dot{\boldsymbol{\mathcal{T}}}_C = \alpha_1 \alpha_2 \dot{\boldsymbol{\mathcal{T}}}_A, \qquad (34)$$

with $\alpha_1 = \exp[i2\pi K_1^0]$ and $\alpha_2 = \exp[i2\pi K_2^0]$ and the uppercase subscripts IJ denoting points along side IJ.

In order to work with the complex-valued displacements of the Bloch wave calculation within the confines of a commercial code, all fields ψ are split into real and imaginary parts,

$$\psi(\mathbf{X}) = \psi^{\text{re}}(\mathbf{X}) + i\psi^{\text{im}}(\mathbf{X}). \qquad (35)$$

In this way the incremental equilibrium [Eq. (10)] splits into two sets of uncoupled equations for the real and imaginary parts,

$$\text{Div } \dot{\boldsymbol{\mathcal{S}}}^{\text{re}} = 0, \quad \text{Div } \dot{\boldsymbol{\mathcal{S}}}^{\text{im}} = 0, \qquad (36)$$

and the problem is solved using two identical finite-element meshes for the primitive cell, one for the real and one for the imaginary part, coupled by Bloch-type displacement boundary conditions (31) that can be rewritten as

$$\dot{\boldsymbol{\kappa}}(\mathbf{X}+\mathbf{R})^{\text{re}} = \dot{\boldsymbol{\kappa}}^{\text{re}}(\mathbf{X})\cos[\mathbf{K}^0 \cdot \mathbf{R}] - \dot{\boldsymbol{\kappa}}^{\text{im}}(\mathbf{X})\sin[\mathbf{K}^0 \cdot \mathbf{R}],$$

$$\dot{\boldsymbol{\kappa}}(\mathbf{X}+\mathbf{R})^{\text{im}} = \dot{\boldsymbol{\kappa}}^{\text{re}}(\mathbf{X})\sin[\mathbf{K}^0 \cdot \mathbf{R}] + \dot{\boldsymbol{\kappa}}^{\text{im}}(\mathbf{X})\cos[\mathbf{K}^0 \cdot \mathbf{R}].$$
$$(37)$$

Similarly, separation of real and imaginary parts in Eq. (33) yields

$$\dot{\boldsymbol{\mathcal{T}}}(\mathbf{X}+\mathbf{R})^{\text{re}} = -\dot{\boldsymbol{\mathcal{T}}}^{\text{re}}(\mathbf{X})\cos[\mathbf{K}^0 \cdot \mathbf{R}] + \dot{\boldsymbol{\mathcal{T}}}^{\text{im}}(\mathbf{X})\sin[\mathbf{K}^0 \cdot \mathbf{R}],$$

$$\dot{\boldsymbol{\mathcal{T}}}(\mathbf{X}+\mathbf{R})^{\text{im}} = -\dot{\boldsymbol{\mathcal{T}}}^{\text{re}}(\mathbf{X})\sin[\mathbf{K}^0 \cdot \mathbf{R}] - \dot{\boldsymbol{\mathcal{T}}}^{\text{im}}(\mathbf{X})\cos[\mathbf{K}^0 \cdot \mathbf{R}].$$
$$(38)$$

Finite-element discretization of Eq. (36) yields

$$\begin{bmatrix} \mathbf{K} & 0 \\ 0 & \mathbf{K} \end{bmatrix} \begin{bmatrix} \hat{\mathbf{v}}^{\text{re}} \\ \hat{\mathbf{v}}^{\text{im}} \end{bmatrix} = \begin{bmatrix} \hat{\mathbf{f}}^{\text{re}} \\ \hat{\mathbf{f}}^{\text{im}} \end{bmatrix}, \qquad (39)$$

where $\mathbf{K}$ represents the full stiffness matrix for the primitive cell $\mathbf{Y}$ and $\hat{\mathbf{v}}^{\text{re}}$, $\hat{\mathbf{v}}^{\text{im}}$, $\hat{\mathbf{f}}^{\text{re}}$ and $\hat{\mathbf{f}}^{\text{im}}$ are the incremental nodal displacements and force vectors corresponding to the discretization of the real and imaginary part of incremental displacements $\dot{\boldsymbol{\kappa}}$ and tractions $\dot{\boldsymbol{\mathcal{T}}}$, respectively. Let us choose the nodal numbering of the primitive cell $\mathbf{Y}$ so that (Fig. 1)

$$\hat{\mathbf{v}} = [\hat{\mathbf{v}}_i \hat{\mathbf{v}}_a \hat{\mathbf{v}}_b]^T, \quad \hat{\mathbf{v}}_a = [\hat{\mathbf{v}}_{AB} \hat{\mathbf{v}}_{AD} \hat{\mathbf{v}}_A]^T,$$

$$\hat{\mathbf{v}}_b = [\hat{\mathbf{v}}_{BC} \hat{\mathbf{v}}_{DC} \hat{\mathbf{v}}_B \hat{\mathbf{v}}_C \hat{\mathbf{v}}_D]^T, \qquad (40)$$

and

$$\hat{\mathbf{f}} = [\hat{\mathbf{f}}_i \hat{\mathbf{f}}_a \hat{\mathbf{f}}_b]^T, \quad \hat{\mathbf{f}}_a = [\hat{\mathbf{f}}_{AB} \hat{\mathbf{f}}_{AD} \hat{\mathbf{f}}_A]^T,$$

$$\hat{\mathbf{f}}_b = [\hat{\mathbf{f}}_{BC} \hat{\mathbf{f}}_{DC} \hat{\mathbf{f}}_B \hat{\mathbf{f}}_C \hat{\mathbf{f}}_D]^T, \qquad (41)$$

with $\hat{\mathbf{v}}_i$ and $\hat{\mathbf{f}}_i$ denoting the degrees of freedom (DOF) of the internal nodes and the force acting on the internal nodes, respectively. Application of incremental displacements [Eq. (37)] and incremental tractions [Eq. (38)] on the boundaries of the cell yields

$$\begin{bmatrix} \hat{\mathbf{v}}^{\text{re}} \\ \hat{\mathbf{v}}^{\text{im}} \end{bmatrix} = [\mathbf{Q}_v] \begin{bmatrix} \hat{\mathbf{v}}_i^{\text{re}} \\ \hat{\mathbf{v}}_a^{\text{re}} \\ \hat{\mathbf{v}}_i^{\text{im}} \\ \hat{\mathbf{v}}_a^{\text{im}} \end{bmatrix}, \qquad (42)$$

and

$$\begin{bmatrix} \hat{\mathbf{f}}^{\text{re}} \\ \hat{\mathbf{f}}^{\text{im}} \end{bmatrix} = [\mathbf{Q}_f] \begin{bmatrix} \hat{\mathbf{f}}_i^{\text{re}} \\ \hat{\mathbf{f}}_a^{\text{re}} \\ \hat{\mathbf{f}}_i^{\text{im}} \\ \hat{\mathbf{f}}_a^{\text{im}} \end{bmatrix}, \qquad (43)$$

where $\mathbf{Q}_v$ and $\mathbf{Q}_f$ contain diagonal block matrices with the sine and cosine factors of Eqs. (37) and (38). Application of conditions (42) and (43) to Eq. (39) and premultiplication by $[\mathbf{Q}_v]^T$ yields

$$\overline{\mathbf{K}} \begin{bmatrix} \hat{\mathbf{v}}_i^{\text{re}} \\ \hat{\mathbf{v}}_a^{\text{re}} \\ \hat{\mathbf{v}}_i^{\text{im}} \\ \hat{\mathbf{v}}_a^{\text{im}} \end{bmatrix} = 0 \qquad (44)$$

since

$$[\mathbf{Q}_v]^T [\mathbf{Q}_f] \begin{bmatrix} \hat{\mathbf{f}}_i^{\text{re}} \\ \hat{\mathbf{f}}_a^{\text{re}} \\ \hat{\mathbf{f}}_i^{\text{im}} \\ \hat{\mathbf{f}}_a^{\text{im}} \end{bmatrix} = 0, \qquad (45)$$

where the matrix $\overline{\mathbf{K}}$,

$$\overline{\mathbf{K}} = [\mathbf{Q}_v]^T \begin{bmatrix} \mathbf{K} & 0 \\ 0 & \mathbf{K} \end{bmatrix} [\mathbf{Q}_v], \qquad (46)$$

is a symmetric function of the Bloch wave vector $\mathbf{K}^0$ and of the loading parameter. Since Eq. (44) represents an eigenvalue problem, the Bloch wave stability analysis of the infinite periodic solid requires finding the first point along the loading path for which the lowest eigenvalue of $\overline{\mathbf{K}}$ is zero. Then the periodicities p_1 and p_2 of the solid at instability are obtained from Eq. (30). Finally we notice that the algorithm can be optimized reducing the size of the eigenvalue problem [Eq. (44)] by static condensation of the degrees of freedom belonging to the internal nodes.[32]

2. Macroscopic instability

In the limiting case of a resulting periodic length of infinity, the microscopic bifurcation can be identified with the start of macroscopic instability and it has been shown that this case corresponds to loss of ellipticity at the macroscopic scale.[31,32] We start by observing that two different types of bifurcation eigenmodes are mapped in the neighborhood of the origin $\mathbf{K}^0$: (i) for $\mathbf{K}^0 = 0$ a periodic "local" mode is found with $p = (1,1)$; (ii) for $\mathbf{K}^0 \to 0$ a "global" long wavelength mode is obtained with wavelength much larger than the unit cell size. The latter case corresponds to loss of ellipticity at the macroscopic scale[32] and it is detected investigating the behavior of the homogenized tangent modulus of the solid $\mathbb{L}^H$,

$$\dot{\bar{\mathbf{S}}} = \mathbb{L}_{ijkl}^H \dot{\bar{\mathbf{F}}}, \quad (47)$$

relating the average rate of the macroscopic deformation gradient $\dot{\bar{\mathbf{F}}}$ to the average rate of the macroscopic first Piola-Kirchoff stress tensor $\dot{\bar{\mathbf{S}}}$.

The infinite periodic solid is said to be strongly elliptic if and only if

$$\mathbb{L}_{ijkl}^H N_j N_l m_i m_k > 0, \quad (48)$$

for all $\mathbf{m} \otimes \mathbf{N} \neq 0$.

Thus loss of ellipticity leading to macroscopic instability occurs when Eq. (48) is violated. Note that the pairs of unit vectors $\mathbf{N}$ and $\mathbf{m}$ for which failure of condition (48) occurs provide information on the instability, $\mathbf{N}$ providing the normal (in the undeformed configuration) to the surface of the discontinuity of the deformation field and $\mathbf{m}$ the type of deformation associated with such a discontinuity (for example, an oblique shear band or an orthogonal collapse band).

Macroscopic instability for the infinite periodically structured solid is investigated using the finite-element method.[29] Operationally, after determining the principal solution the components of $\mathbb{L}^H$ are identified by subjecting the unit cells to four independent linear perturbations of the macroscopic deformation gradient, calculating the corresponding averaged stress components and comparing to Eq. (47). Then loss of ellipticity is examined by checking condition (48) at every $\pi/720$ radian increment.

Note that for the infinite monolithic solid subjected to macroscopic deformation the deformation is homogeneous, so that $\mathbb{L}^H$ is coincident with $\mathbb{L}$ as defined in Eq. (12) and loss of ellipticity can be investigated analytically. Finally we observe that the macroscopic critical load is always greater than or equal to the microscopic critical load, with the equality achieved when, in the microscopic analysis, the critical load is obtained for $\mathbf{K}^0 \rightarrow 0$.

3. Wave propagation

For the infinite periodically structured solid the finite-element method is used to investigate the propagation of acoustic waves through the predeformed material,[13,30] yielding a formulation similar to that presented for the investigation of their corresponding microscopic instability. First, to work with the complex valued displacements of the Bloch wave calculation within the confines of a commercial code, all fields are split into real and imaginary parts [see Eq. (35)]. In this way the incremental equations of motion [Eq. (17)] split into two sets of uncoupled equations for the real and imaginary parts,

$$\mathrm{Div}\ \dot{\boldsymbol{\mathcal{S}}}^{\mathrm{re}} + \rho_0 \omega^2 \dot{\boldsymbol{\kappa}}^{\mathrm{re}} = 0,$$

$$\mathrm{Div}\ \dot{\boldsymbol{\mathcal{S}}}^{\mathrm{im}} + \rho_0 \omega^2 \dot{\boldsymbol{\kappa}}^{\mathrm{im}} = 0. \quad (49)$$

The problem is then solved using two identical finite-element meshes for the cell, one for the real part and one for the imaginary part and coupling them by Bloch-type displacement boundary conditions given by Eq. (37). Finite-element formulation of Eq. (49) yields

$$\left(\begin{bmatrix} \mathbf{K} & 0 \\ 0 & \mathbf{K} \end{bmatrix} - \omega^2 \begin{bmatrix} \mathbf{M} & 0 \\ 0 & \mathbf{M} \end{bmatrix} \right) \begin{bmatrix} \hat{\mathbf{v}}^{\mathrm{re}} \\ \hat{\mathbf{v}}^{\mathrm{im}} \end{bmatrix} = \begin{bmatrix} \hat{\mathbf{f}}^{\mathrm{re}} \\ \hat{\mathbf{f}}^{\mathrm{im}} \end{bmatrix}, \quad (50)$$

where the submatrices $\mathbf{K}$ and $\mathbf{M}$ are the tangent stiffness and mass matrices of a single mesh, respectively. Substitution of Eqs. (42) and (43) and premultiplication by $[\mathbf{Q}_v]^T$ yields

$$[\mathbf{Q}_v]^T \left(\begin{bmatrix} \mathbf{K} & 0 \\ 0 & \mathbf{K} \end{bmatrix} - \omega^2 \begin{bmatrix} \mathbf{M} & 0 \\ 0 & \mathbf{M} \end{bmatrix} \right) [\mathbf{Q}_v] \begin{bmatrix} \hat{\mathbf{v}}_i^{\mathrm{re}} \\ \hat{\mathbf{v}}_a^{\mathrm{re}} \\ \hat{\mathbf{v}}_i^{\mathrm{im}} \\ \hat{\mathbf{v}}_a^{\mathrm{im}} \end{bmatrix} = 0, \quad (51)$$

where condition (45) has been used. Thus eigenfrequencies ω can be computed from Eq. (51) for any wave vector $\mathbf{K}^0$. Here waves propagating in the $x_1 - x_2$ plane are considered, so that $K_3^0 = 0$ and the decoupling between the out-of-plane x_3 and in-plane $x_1 - x_2$ wave polarizations is obtained. Differently when oblique propagation of elastic waves in phononic crystals is considered,[34] all three polarizations of the displacement field are fully coupled.

III. RESULTS

First, the case of an infinite monolithic hyperelastic solid is considered (Sec. III C). This problem is used to compare the analytical solution for the effect of deformation and stress on the propagation of acoustic waves [Eqs. (20)–(22)] to its numerical implementation [Eq. (51)] as well as to examine the influence of the postulated hyperelastic constitutive law on this behavior.

Second, results for infinite periodically structured elastomeric solids are presented. Instabilities and propagation of acoustic waves for a square array of circular holes in a compressible neo-Hookean matrix subjected to uniaxial compression have been recently investigated[28–30] and the results are summarized in Sec. III D 1. Here, the effects of different loading conditions (Sec. III D 2), different material properties (Sec. III D 3), different shape of the holes (Sec. III D 4) and inclusions (Sec. III D 5) are investigated, showing different possibilities for tuning and manipulating the location and presence of both the instability and the phononic gaps.

The nonlinear finite-element code ABAQUS/STANDARD is used to deform the structures as well as to obtain the dispersion diagrams. For the instability analysis and the simulation of the stress-strain behavior, a two-dimensional (2D) mesh is constructed for each primitive cell using 6-node hybrid elements (elements CPE6H in ABAQUS). Differently, to investigate the propagation of elastic waves through the structures a three-dimensional (3D) mesh of each representative volume element (RVE) is constructed using 15-node hybrid wedge elements (elements C3D15H in ABAQUS), so that the propagation of waves within the plane and out-of the plane polarization is investigated.

A. Constituent material properties

The matrix is modeled as an almost incompressible elastomeric material. Its behavior is described using the com-

pressible version of the strain energy density proposed by Gent,[35]

$$W(I_1,J) = -\frac{\mu}{2}J_m \log\left(1 - \frac{I_1-3}{J_m}\right) - \mu \log J$$
$$+ \left(\frac{K}{2} - \frac{\mu}{J_m}\right)(J-1)^2, \quad (52)$$

where μ and K are the initial shear and bulk moduli, respectively. J_m in Eq. (52) is a constant related to the strain saturation of the material, since the stresses become infinite as $(J_m - I_1 + 3)$ approaches zero. The first Piola-Kirchoff stress $\mathbf{S} = \partial W / \partial \mathbf{F}$ is then found as

$$\mathbf{S} = \frac{\mu J_m}{J_m - I_1 + 3}\mathbf{F} + J\left[\left(K - \frac{2\mu}{J_m}\right)(J-1) - \frac{\mu}{J}\right]\mathbf{F}^{-T}, \quad (53)$$

and $\mathbb{L} = \partial^2 W / \partial \mathbf{F} \partial \mathbf{F}$ is given by

$$\mathbb{L} = \frac{\mu J_m}{J_m - I_1 + 3}\mathbb{I} + \frac{2\mu J_m}{(J_m - I_1 + 3)^2}\mathbf{F} \otimes \mathbf{F}$$
$$+ J(2J-1)\left(K - \frac{2\mu}{J_m}\right)\mathbf{F}^{-T} \otimes \mathbf{F}^{-T}$$
$$+ \left[J(J-1)\left(K - \frac{2\mu}{J_m}\right) - \mu\right]\mathbb{A}, \quad (54)$$

with

$$\mathbb{I}_{ijkl} = \frac{\partial F_{ij}}{\partial F_{kl}} = \delta_{ik}\delta_{jl}, \quad (55)$$

δ_{ij} denoting the Kronecker delta and

$$\mathbb{A}_{ijkl} = \frac{\partial F_{ij}^{-T}}{\partial F_{kl}} = -F_{il}^{-T}F_{kj}^{-T}. \quad (56)$$

Note that for $J_m \to \infty$ the Gent energy density in Eq. (52) converges to the neo-Hookean energy density

$$W(I_1,J) = \frac{\mu}{2}(I_1 - 3) - \mu \log J + \frac{K}{2}(J-1)^2, \quad (57)$$

so that $\mathbf{S}$ and $\mathbb{L}$ are given by

$$\mathbf{S} = \mu\mathbf{F} + J\left[K(J-1) - \frac{\mu}{J}\right]\mathbf{F}^{-T}, \quad (58)$$

and

$$\mathbb{L} = \mu\mathbb{I} + KJ(2J-1)\mathbf{F}^{-T} \otimes \mathbf{F}^{-T} + [J(J-1)K - \mu]\mathbb{A}, \quad (59)$$

respectively.

Here for the elastomeric matrix an initial shear modulus μ of 1.08 MPa and bulk modulus K of 2 GPa are considered and both the case of a neo-Hookean behavior ($J_m \to \infty$) and a Gent behavior with different values of J_m are investigated. The initial elastomer density is 1.050 g/cm³. The material properties are chosen to correspond to those describing the behavior of PSM-4 (Refs. 29 and 30) in the case of $J_m \to \infty$. Notice that in the undeformed configuration the incremental moduli tensors $\mathbb{L}$ for the Gent material [Eq. (54)] and the neo-Hookean material [Eq. (59)] are the same, so that both

TABLE I. Material properties for the matrix and the inclusions: density ρ_0, shear modulus μ, bulk modulus K, c_{t0} and c_{l0}.

Material	ρ_0 (g/cm³)	μ (GPa)	K (GPa)	J_m	c_{t0} (m/s)	c_{l0} (m/s)
Matrix: neo-Hookean	1.05	0.00108	2	∞	32	1311
Matrix: Gent	1.05	0.00108	2	J_m	32	1311
Inclusions: gold (Au)	19.3	28.73	230	∞	1220	3859

materials are characterized by an initial transverse speed of sound $c_{t0} = \sqrt{\mu/\rho_0} = 32.1$ m/s and an initial longitudinal speed of sound $c_{l0} = \sqrt{(K+2\mu)/\rho_0} = 1312$ m/s as listed in Table I.

To provide strong contrast in density between the matrix and inclusions, the inclusions are chosen to be made of gold. Gold is characterized by an initial shear modulus μ of 28.7 GPa, a bulk modulus K of 230 GPa, and an initial density ρ_0 of 19.3 g/cm³. Although the stress-strain behavior of gold is elasto-plastic, the stress level experienced by the material in the simulations presented here is such that its behavior can be accurately described using the neo-Hookean model (58).

B. Loading conditions

The following macroscopic loading conditions are considered:

(i) a plane strain compression/tension in the x_2 direction, so that the macroscopic deformation gradient $\overline{\mathbf{F}}$ is given by

$$\overline{\mathbf{F}} = \tilde{\lambda}\hat{\mathbf{e}}_1 \otimes \hat{\mathbf{e}}_1 + \lambda\hat{\mathbf{e}}_2 \otimes \hat{\mathbf{e}}_2 + \hat{\mathbf{e}}_3 \otimes \hat{\mathbf{e}}_3, \quad (60)$$

λ denoting the applied stretch and $\tilde{\lambda}$ being determined from the constraint $S_{11} = 0$;

(ii) a plane strain equibiaxial compression/tension, so that the macroscopic deformation gradient $\overline{\mathbf{F}}$ is given by

$$\overline{\mathbf{F}} = \lambda\hat{\mathbf{e}}_1 \otimes \hat{\mathbf{e}}_1 + \lambda\hat{\mathbf{e}}_2 \otimes \hat{\mathbf{e}}_2 + \hat{\mathbf{e}}_3 \otimes \hat{\mathbf{e}}_3, \quad (61)$$

λ denoting the applied stretch;

(iii) simple shear, so that the macroscopic deformation gradient $\overline{\mathbf{F}}$ is given by

$$\overline{\mathbf{F}} = \hat{\mathbf{e}}_1 \otimes \hat{\mathbf{e}}_1 + \hat{\mathbf{e}}_2 \otimes \hat{\mathbf{e}}_2 + \hat{\mathbf{e}}_3 \otimes \hat{\mathbf{e}}_3 + \tan\gamma\hat{\mathbf{e}}_1 \otimes \hat{\mathbf{e}}_2, \quad (62)$$

γ denoting the shear angle.

To subject a representative volume element to the macroscopic deformation gradient $\overline{\mathbf{F}}$, periodic boundary conditions are imposed on all cell boundaries such that

$$\mathbf{u}_B - \mathbf{u}_A = (\overline{\mathbf{F}} - \mathbf{I})(\mathbf{X}_B - \mathbf{X}_A) = \overline{\mathbf{H}}(\mathbf{X}_B - \mathbf{X}_A), \quad (63)$$

where A and B are two points periodically located on the RVE boundary. In Eq. (63) $\overline{\mathbf{H}}$ denotes the macroscopically applied displacement gradient and $\mathbf{u} = \mathbf{x}(\mathbf{X}) - \mathbf{X}$ denotes the displacement at X. The macroscopic deformation is imposed by prescribing the four components of $\overline{\mathbf{H}}$, which are viewed as generalized degrees of freedom operationally applied using a set of virtual nodes. The macroscopic first Piola-Kirchoff stress tensor is then extracted through virtual work considerations.[36] Rigid body motion is prevented by constraining the displacements of a single point.
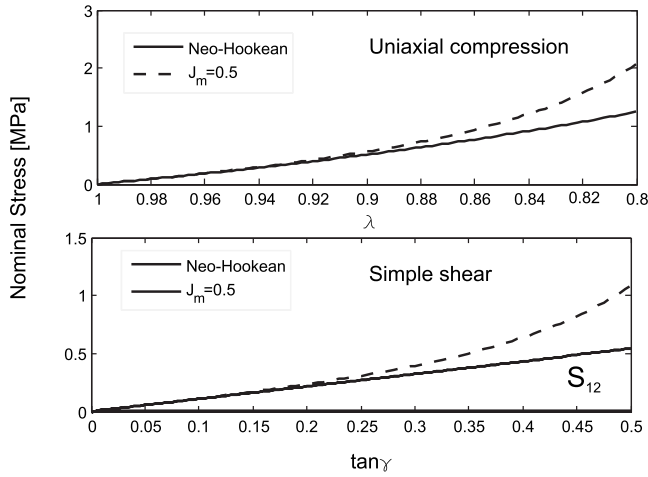
FIG. 2. Nominal stress curves during uniaxial compression in vertical direction (top) and simple shear (bottom) for an infinite homogeneous body. Both the case of a neo-Hookean material and of a Gent material with $J_m=0.5$ are reported.

C. Effect of prestress on wave propagation in hyperelastic monolithic solid

Monolithic neo-Hookean and Gent solids with $J_m=0.5$ are subjected to plane strain compression in the x_2 direction and simple shear. For both materials loss of ellipticity along the loading path does not occur during uniaxial and shear loading. Here, the effects of the two different deformation fields on the stress-strain behavior and on the propagation of acoustic waves are analytically investigated.

1. Stress-strain behavior

Figure 2 shows the influence of the material constitutive law on the stress-strain response of the monolithic elastomer subjected to uniaxial compression (top) and simple shear (bottom). The effect of the Gent material stiffening (taking $J_m=0.5$) with strain clearly appears for uniaxial loading when $\lambda < 0.9$ and for simple shear when $\tan \gamma > 0.2$.

2. Propagation of acoustic waves

Figure 3 presents the phononic band diagrams for the monolithic neo-Hookean solid (top) and the monolithic Gent solid (bottom) in the undeformed configuration. Both in-plane $x_1 - x_2$ (on the left part of each band diagram) and out-of-plane x_3 (on the right part of each band diagram) modes are shown. On the vertical axis the nondimensional eigenfrequencies $\tilde{\omega} = \omega A / (2\pi c_{t0})$ are reported with $A = (\|\mathbf{A}_1\| + \|\mathbf{A}_2\|)/2$, while on the horizontal axis the magnitude of the Bloch wave vector is reported. Analytical results (continuous lines) are compared to numerical results (markers) showing an excellent agreement. For the numerical analyses a square cell is used as shown in Fig. 3 (left). Notice that for square cells, the wave equation only has to be calculated for Bloch wave vector values along the curve G-L-M-G (Fig. 3—left). Analytical results are obtained from Eq. (20) and the various eigenmodes are obtained considering Bloch wave vectors
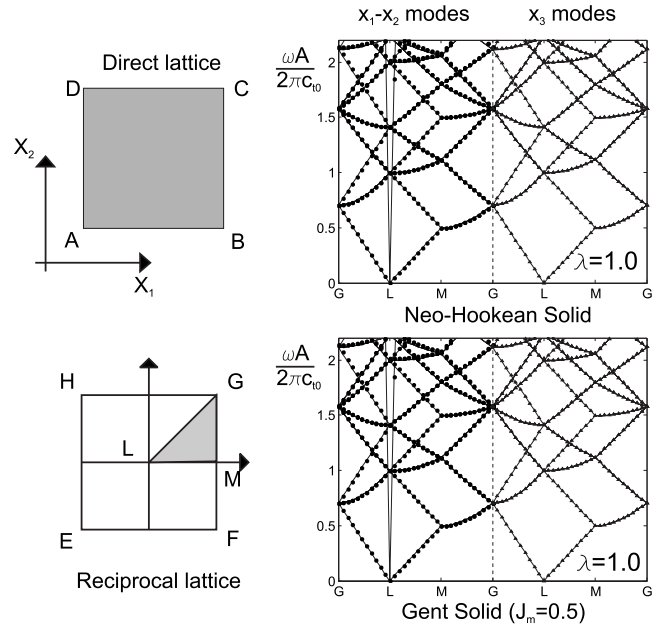

FIG. 3. Phononic band-gap structure for the monolithic solid in the undeformed configuration: neo-Hookean material (top) and Gent material with $J_m=0.5$ (bottom). In-plane (labeled $x_1 - x_2$) and out-of-plane (labeled x_3) modes are reported on the left and right part of the plots. The points G, L, and M are defined on the left.

$$\widetilde{\mathbf{K}}^0 = \frac{2\pi n_1}{\|\mathbf{A}_1\|} K_1^0 \mathbf{B}_1 + \frac{2\pi n_2}{\|\mathbf{A}_2\|} K_2^0 \mathbf{B}_2, \tag{64}$$

where n_1 and n_2 denote integers.

As expected, the band diagrams of both the Gent and the neo-Hookean solid in the undeformed configuration are the same since the two materials have the same incremental tangent moduli $\mathbb{L}$ when undeformed. The band diagrams for the two solids subjected to uniaxial compression at $\lambda=0.8$ and to simple shear at $\tan \gamma=0.3$ are reported in Figs. 4 and 5, respectively. Although both materials are still characterized by the absence of both in-plane $x_1 - x_2$ and out-of-plane x_3 phononic band gaps, there is a clear difference between their band diagrams when deformed. Comparison of Fig. 3 with Figs. 4 and 5 clearly shows that the deformation has a negligible effect on wave propagation in the neo-Hookean material, while the dispersion curves of the Gent solid are strongly influenced by the deformation. In the Gent solid deformation induces privileged directions (and thus anisotropy) inside the material, whose influence on the dispersion curves should not be neglected.

D. Square array of circular holes subjected to deformation

1. Uniaxial compression

An infinitely repeating square array of circular holes in a neo-Hookean matrix subjected to uniaxial compression in the x_2 direction is considered (Fig. 6). The periodic structure is characterized by an initial volume fraction $f_0=0.6$. The primitive cell **Y** is defined by the lattice vectors $\mathbf{A}_1 = [R_0\sqrt{\pi/f_0} \ \ 0]$ and $\mathbf{A}_2 = [0 \ \ R_0\sqrt{\pi/f_0}]$, with R_0 denoting the initial radius of the circular voids.
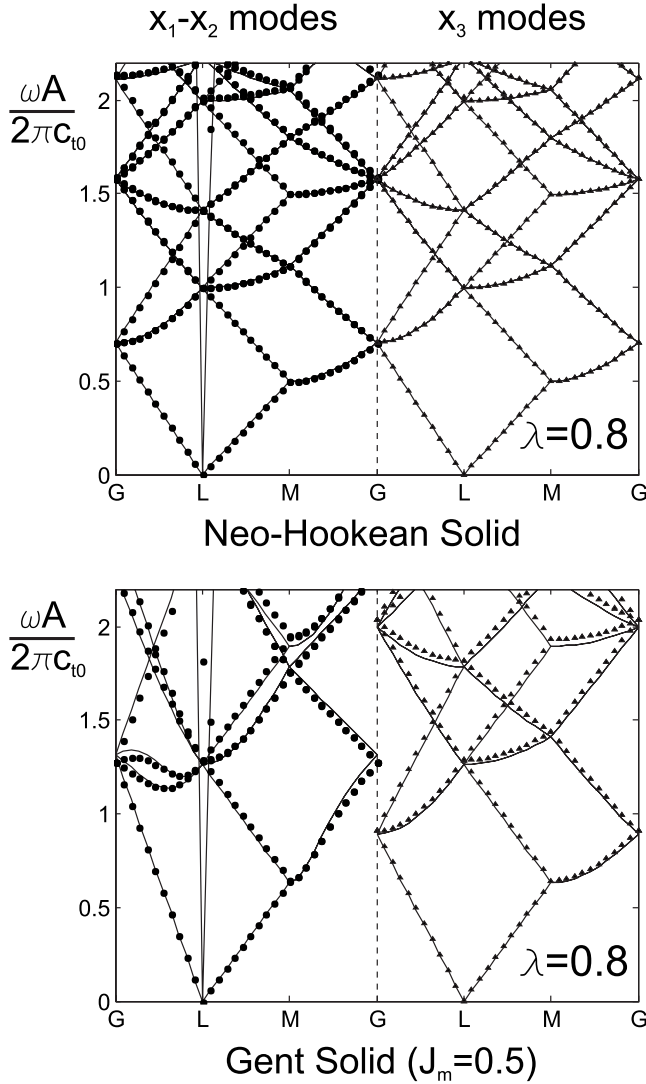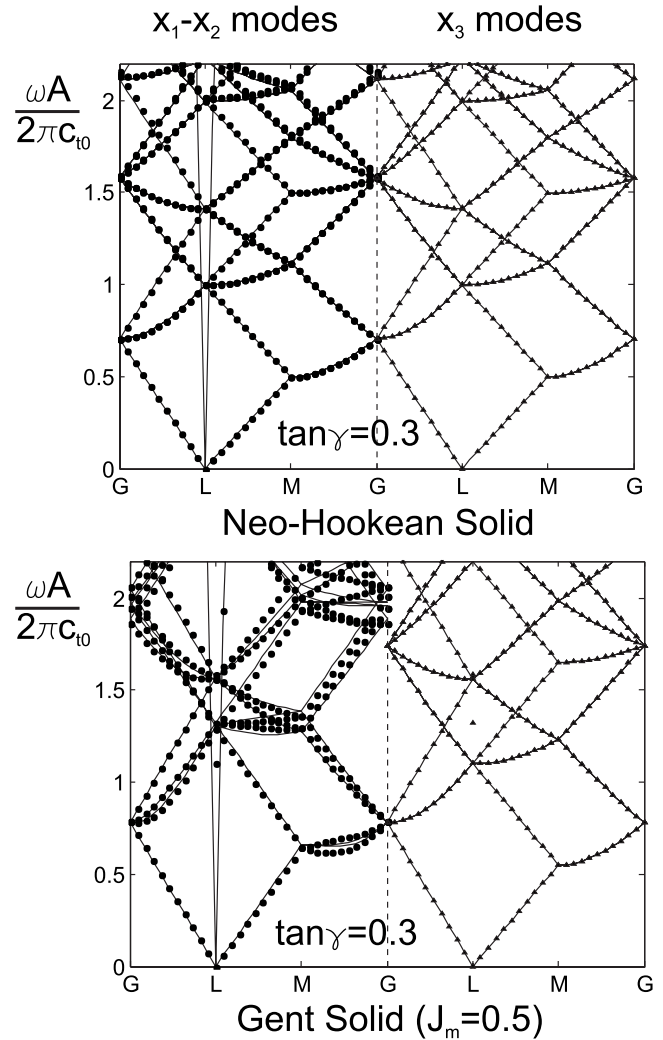
FIG. 4. Phononic band-gap structure for the monolithic solid subjected to uniaxial compression: neo-Hookean material (top) and Gent material with $J_m=0.5$ (bottom). In-plane (labeled x_1-x_2) and out-of-plane (labeled x_3) modes are reported on the left and right part of the plots. The points G, L, and M are defined in Fig. 3.

a. Analysis of instability. Bloch wave analyses performed on the primitive cell (Fig. 6—right) during compression simulations detected a critical instability at $\lambda=0.965$. When the critical instability occurs, the **Y** periodicity is broken and an enlarged primitive cell **p**-**Y** with $p=(2,2)$ is found, as shown in Fig. 7.

If the first eigenmode were suppressed, then loss of ellipticity for the homogenized tangent modulus is encountered at $\lambda=0.943$, leading to macroscopic instability. Failure of the strong ellipticity condition (48) occurs when $\mathbb{L}^H_{1212}$ vanishes, implying $\mathbf{N}=[0 \ 1]$ and $\mathbf{m}=[1 \ 0]$. Thus at macroscopic instability a collapse band normal to the direction of the applied load appears. Further we observe that the microscopic instability suppresses the formation of collapse bands (i.e., loss of ellipticity does not occur before complete closure of the pores).

b. Stress-strain behavior. Load-displacement analyses for

FIG. 5. Phononic band-gap structure for the monolithic solid subjected to simple shear: neo-Hookean material (top) and Gent material with $J_m=0.5$ (bottom). In-plane (labeled x_1-x_2) and out-of-plane (labeled x_3) modes are reported on the left and right part of the plots. The points G, L, and M are defined in Fig. 3.

the infinite periodic structure are performed with ABAQUS/ STANDARD. Since the periodic solid is characterized by a critical microscopic instability with periodicity of two along both lattice directions, a **p**-**Y** cell with $\mathbf{p}=(2,2)$ is used and a geometrical imperfection with the form of the first eigenmode is introduced to preferentially activate the first mode during the simulation and to capture the post-transformation
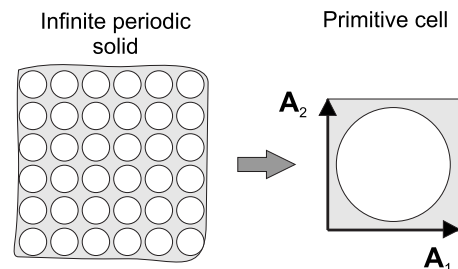

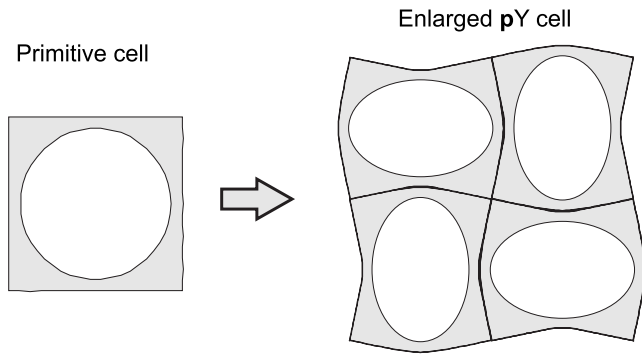FIG. 6. Inifinite square array of circular voids.

FIG. 7. Eigenmode of the microscopic bifurcation instability for the square array of circular holes as predicted by the Bloch wave analysis.

behavior. Figure 8 shows the stress-strain behavior for the infinite square array of circular holes subjected to uniaxial compression in x_2 direction. The porous solid is characterized by an initial linear response with a sudden departure from linearity to a plateau region after the instability occurs. During the initial linear elastic response of the periodic structure, the circular holes are observed to undergo a gradual and homogeneous compression (Fig. 9, top and left). The plateau region corresponds to a homogeneous pattern transformation to a pattern of alternating mutually orthogonal ellipses that is accentuated with increasing deformation as shown in Fig. 9 (bottom and left).

c. Propagation of acoustic waves. The band diagrams for the porous structure are provided in Fig. 9 at different levels of macroscopic stretch λ. The transformation of the band gaps with deformation is reported in Fig. 10. In the undeformed configuration, the periodic structure possesses an inplane $x_1 - x_2$ phononic band gap for normalized frequencies of $\tilde{\omega} = 0.61 - 0.82$ and an intersecting out-of-plane x_3 gap for $\tilde{\omega} = 0.45 - 0.68$, yielding a complete phononic band gap for $\tilde{\omega} = 0.61 - 0.68$ (Fig. 9, top). During the initial linear elastic response of the periodic structure, the band gaps are affected marginally by the deformation, evolving in an affine and monotonic manner (Fig. 10). When pattern transformation occurs, the in-plane $x_1 - x_2$ modes undergo a transformation as well, while the out-of-plane x_3 modes are observed to be only marginally affected by the pattern transformation. A new in-plane $x_1 - x_2$ band gap is opened at $\tilde{\omega} = 2$, and the preexisting gap now begins to widen.
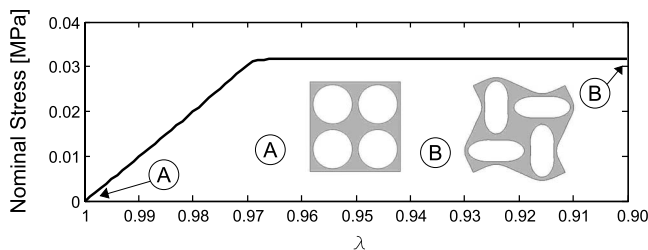

FIG. 8. Nominal stress vs applied stretch λ curve during uniaxial compression in vertical direction for the square array of circular holes.
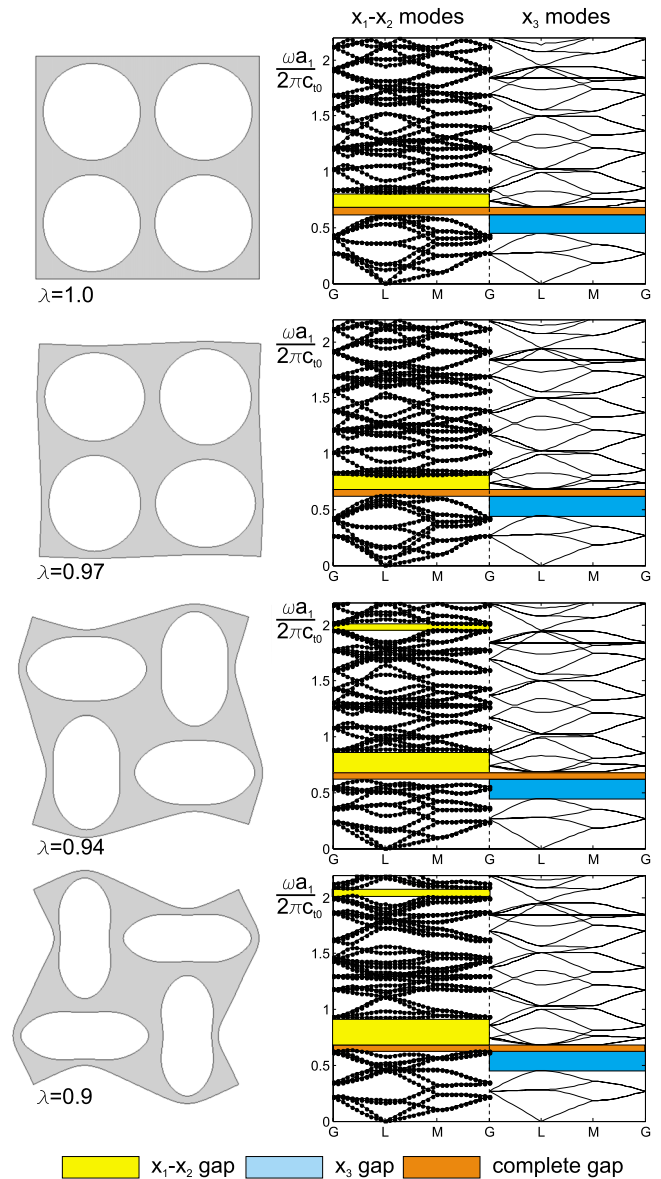

FIG. 9. (Color online) Phononic band-gap structure for the square array of circular void in a neo-Hookean matrix subjected to uniaxial compression at different levels of macroscopic deformation. In-plane (labeled $x_1 - x_2$) and out-of-plane (labeled x_3) modes are reported on the left and right part of the plots. The points G, L, and M are defined in Fig. 3.

2. Different loading conditions

The effects of different loading conditions (uniaxial compression, uniaxial tension, equibiaxial compression, equibiaxial tension and simple shear) on both instability and propagation of acoustic waves are presented for the case of the square array of circular voids.

a. Analysis of instability. Table II reports the values of the applied stretch λ_{micro} at microscopic instability and λ_{macro} at macroscopic instability (loss of ellipticity for the homogenized tangent modulus) for the cases of uniaxial compression, uniaxial tension, equibiaxial compression, equibiaxial tension, and simple shear. Both microscopic and macro-
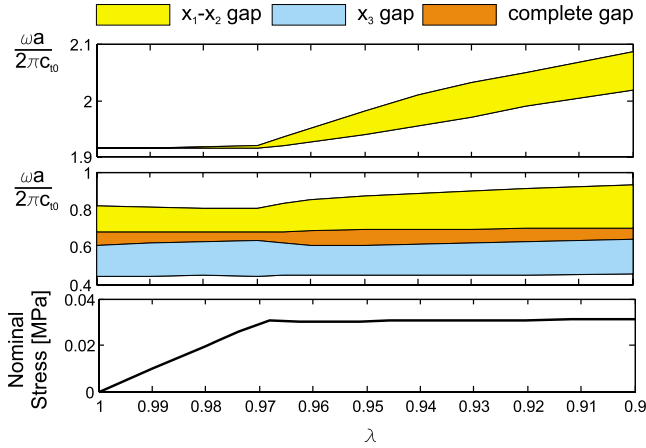
FIG. 10. (Color online) Phononic band gap (top and center) and nominal stress (bottom) vs applied stretch λ for the square array of circular void in a neo-Hookean matrix subjected to uniaxial compression.

scopic instabilities are observed to occur at smaller compression strain (larger compression stretch) for the case of equibiaxial compression as compared to that found for uniaxial compression. The microscopic instability is characterized by the same eigenmode and periodicity found in the case of uniaxial compression (Fig. 7). If the first eigenmode is suppressed, macroscopic instability occurs when $\mathbb{L}_{1212}^{H}$ and $\mathbb{L}_{2121}^{H}$ vanish, implying $\mathbf{N}=[0\ 1]$ and $\mathbf{m}=[1\ 0]$, and $\mathbf{N}=[1\ 0]$ and $\mathbf{m}=[0\ 1]$. Thus at failure two collapse bands perpendicular to each other and parallel to the principal directions of the stress tensor appear. Similarly as for the case of uniaxial compression, microscopic instability is observed to suppress macroscopic instability. Differently, when the structure is subjected to uniaxial tension, simple shear, and equibiaxial tension no macroscopic or microscopic instability is observed. Microscopic and macroscopic instabilities have been observed for an infinite square array of circular holes with a void volume fraction of $\pi/16$ subjected to equibiaxial tension,[37] but they do not occur for the larger void volume fraction considered here. However, assuming an initial void volume fraction $f_0=0.2$, a microscopic instability is detected at $\lambda=2.5$ during equibiaxial tension simulations. This instability results in an enlarge primitive cell $\mathbf{p}-\mathbf{Y}$ with $p=(2,2)$ consisting of holes with alternating large and small

TABLE II. Critical stretch λ_{micro} at microscopic instability and λ_{macro} at macroscopic instability.

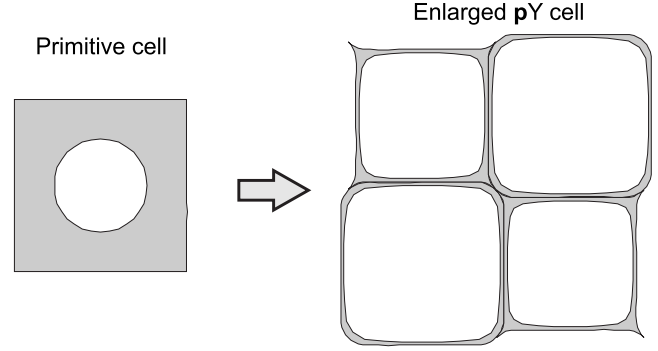|	λ_{micro}	λ_{macro}
Uniaxial compression	0.965	0.943
Uniaxial tension	—	—
Equibiaxial compression	0.9880	0.964
Equibiaxial tension	—	—
	$\tan\gamma_{\text{micro}}$	$\tan\gamma_{\text{macro}}$
Shear	—	—

FIG. 11. Eigenmode of the microscopic bifurcation instability for the square array of circular holes with $f_0=0.2$ subjected to equibiaxial tension as predicted by the Bloch wave analysis.

dimensions, as shown in Fig. 11. However, this microscopic instability occurs as such large strain that it is difficult to obtain experimentally since the interhole ligaments are too highly stretched and therefore is not further investigated here.

b. Stress-strain behavior. The stress-stretch behavior of the infinite periodic solid subjected to uniaxial and equibiaxial compression is reported in Fig. 12 (top). In both cases an initial linear response is followed by a plateau region as the result of the pattern transformation occurring after instability. Differently, for uniaxial and equibiaxial tension (Fig. 12, center) and for simple shear (Fig. 12, bottom), due the absence of microscopic instability, no sharp discontinuity in the stress-strain response is observed.
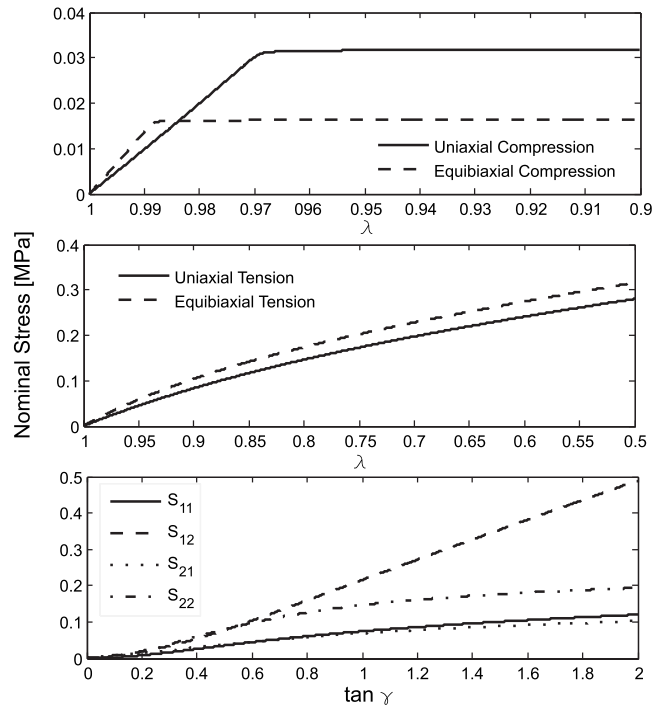

FIG. 12. Nominal stress response during uniaxial compression in vertical direction and equibiaxial compression (top), uniaxial tension in vertical direction and equibiaxial tension (center) and simple shear (bottom) for the square array of circular holes in a neo-Hookean matrix.
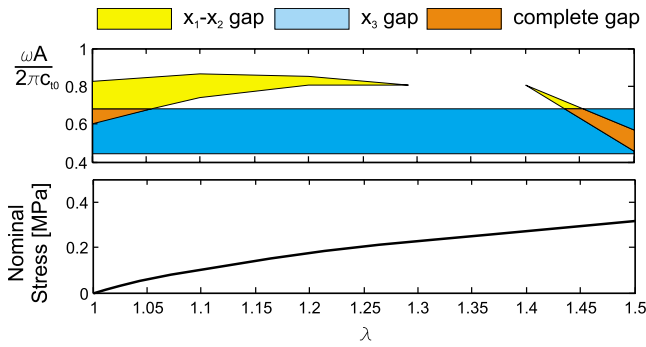
FIG. 13. (Color online) Phononic band gap (top) and nominal stress (bottom) vs applied stretch λ for the square array of circular holes subjected to equibiaxial tension.

c. Propagation of acoustic waves. The band diagrams for the square array of circular voids subjected to equibiaxial compression and the evolution of the phononic band gaps with deformation show features similar to that observed for uniaxial compression. Figure 13 shows the transformation of the phononic band gaps with deformation when the periodic solid is subjected to equibiaxial tension. Since no microscopic instability occurs for equibiaxial tension, the wave propagation is investigated considering a RVE consisting of a single primitive cell. The first in-plane band gap is observed to reduce progressively its width with deformation up to closure occurring at $\lambda = 1.3$ and then to reopen at $\lambda = 1.4$ and to decrese its frequency with further increase in strain. Finally, the evolution of the phononic band gaps with deformation is shown in Fig. 14. Figures 13 and 14 clearly show that for the cases of both equibiaxial tension and simple shear much larger strains than for the cases of uniaxial or equibiaxial compression need to be applied to the structures to affect the phononic band gaps of the solids. This behavior is a consequence of the absence of pattern transformation along the loading path for the periodic structures subjected to equibiaxial tension and simple shear and indicates that the
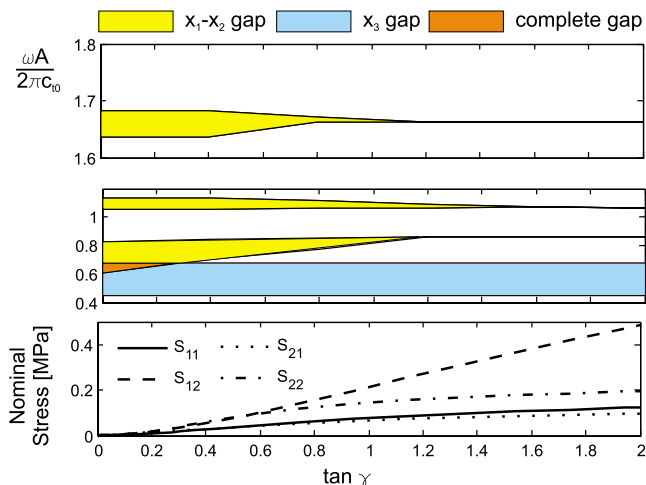

FIG. 14. (Color online) Phononic band gap (top and center) and nominal stress (bottom) vs $\tan \gamma$ for the square array of circular voids in a neo-Hookean matrix.
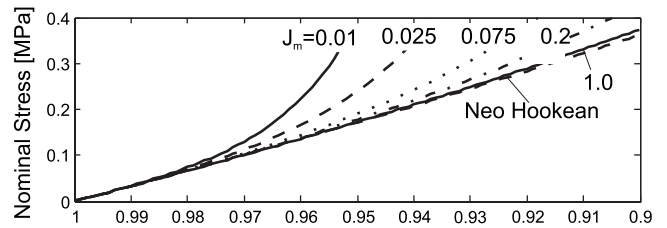

FIG. 15. Nominal stress vs applied stretch λ curves for $J_m = [0.01, 0.025, 0.075, 0.2, 1, \infty]$ for the monolithic Gent material subjected to uniaxial compression.

phononic band gaps in a porous neo-Hookean structure are mainly governed by the shape and the volume fraction of the pores.

3. Effect of matrix material properties

The influence of the matrix constitutive law on the response of the square array of circular voids is investigated by varying the stiffening parameter J_m. The effect of J_m on the stress-stretch behavior of the monolithic Gent solid subjected to uniaxial compression is reported in Fig. 15. Low values of J_m are found to cause the stress behavior to stiffen at large values of the applied stretch λ.

a. Analysis of instability. Figure 16 shows the evolution of both λ_{micro} (top) and λ_{macro} (bottom) as a function of the material parameter J_m for the square array of circular holes subjected to uniaxial compression in the x_2 direction. For J_m below 0.02, stiffening of the elastomeric matrix occurs before both microscopic and macroscopic instability. For J_m above 0.02 and below 0.04 microscopic instability is suppressed, so that macroscopic instability occurs first, resulting in a collapse band normal to the direction of loading. Finally for J_m above 0.02 microscopic instability with a periodicity $p = (2,2)$ and the same eigenmode as for the period solid (Fig. 7) occurs first, suppressing macroscopic instability. Clearly increasing the parameter J_m, the material behavior tends to that characterizing the neo-Hookean solid and for J_m above 1 both macroscopic and microscopic instability are
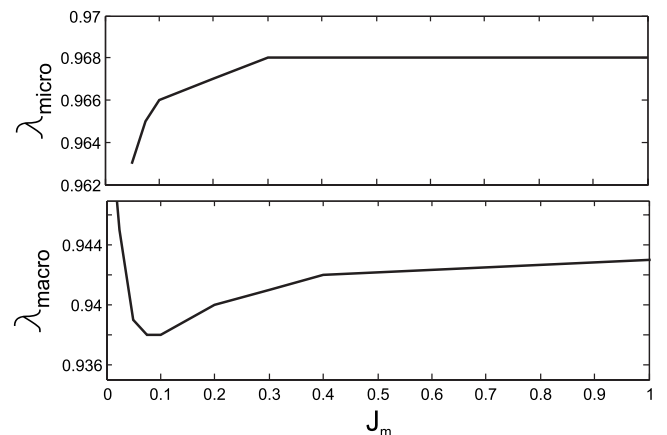

FIG. 16. Evolution of λ_{micro} (top) and λ_{macro} (bottom) as a function of J_m for the square array of circular holes in a Gent elastomeric matrix.
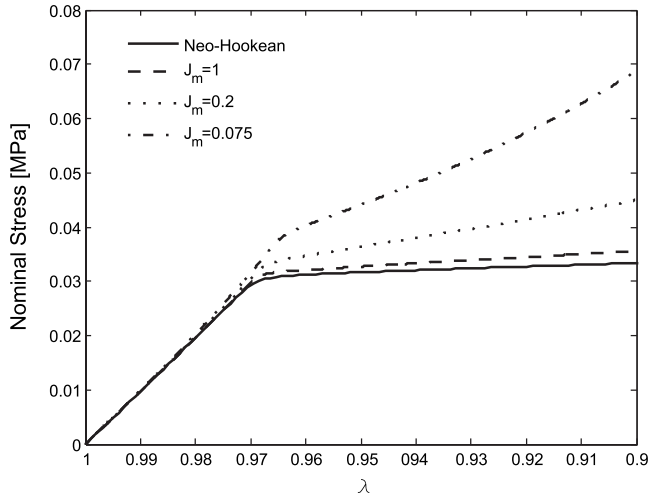
FIG. 17. Nominal stress vs applied stretch λ curves for J_m $=[0.075, 0.2, 1, \infty]$ for the square array of circular voids in a Gent elastomeric matrix subjected to uniaxial compression.

observed to occur at the same value of applied stretch λ as for the periodic structure with a neo-Hookean material.

b. Stress-strain behavior. The stress-strain behavior of the square array of circular voids is reported in Fig. 17 for $J_m=[0.075, 0.2, 1, \infty]$. For $J_m=0.075$ and $J_m=0.2$ the stress is observed not to plateau after the critical instability due to the stiffening effect. However the same pattern of alternating, mutually orthogonal ellipses is observed to develop (Fig. 9—left).

c. Propagation of acoustic waves. The propagation of acoustic waves through the structure is evaluated at different levels of macroscopic deformation for the case of J_m $=0.075$. The transformation of the band gaps with deformation is reported in Fig. 18. Although the neo-Hookean and the Gent periodic structures have the same band diagrams in the undeformed configuration, a comparison of Fig. 18 with Fig. 10 reveals that the gaps for the two materials evolve differently. For the Gent solid with $J_m=0.075$ the full band gap is observed to completely close when the instability occurs, since the first in-plane band gap is found not only to widen but also to change its location. An additional band gap opens at $\lambda=0.97$ as an effect of the constitutive stiffening of the elastomeric matrix. Finally, the Gent porous solid shows a small effect of deformation also on the out-of-plane band gap; when pattern transformation occurs, the out-of-plane band gap decreases its width gradually. In conclusion, the stiffening effect characterizing the elastomeric material is found to strongly influence the band gaps of the periodic structure with deformation. For the Gent solid the phononic band gaps are governed not only by the shape of the pores, but also the privileged directions induced inside the elastomeric material by the deformation play an important role.

4. Effect of void shape

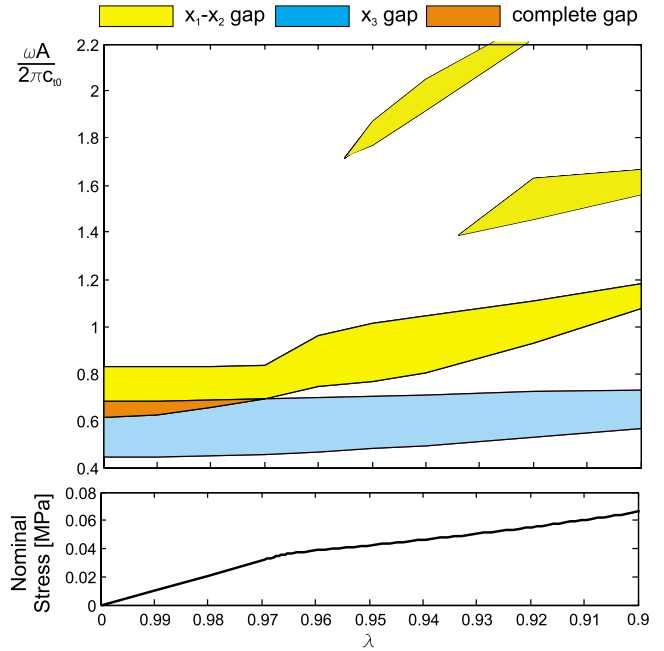An infinite square array of circular voids in a neo-Hookean matrix with an initial volume fraction $f_0=0.6$ sub-

FIG. 18. (Color online) Phononic band gap (top) and nominal stress (bottom) vs applied stretch λ for the square array of circular voids in a Gent elastomeric matrix with $J_m=0.075$ subjected to uniaxial compression.

jected to uniaxial compression in the x_2 direction is considered, as in Sec. III D 1. The effect of voids with an elliptical shape is investigated by considering voids with different aspect ratio E_2/E_1, where E_2 and E_1 denote the two semiaxes of the ellipse. The semiaxes and the dimensions of the primitive cell are chosen so that the initial volume fraction is held constant at $f_0=0.6$ and such that $\|\mathbf{A}_1\|-E_1=\|\mathbf{A}_2\|-E_2$.

a. Analysis of instability. Figure 19 reports the evolution of λ at both microscopic and macroscopic instability as a function of the ellipse aspect ratio E_2/E_1. Microscopic instability with a periodicity $p=(2,2)$ is observed to occur first
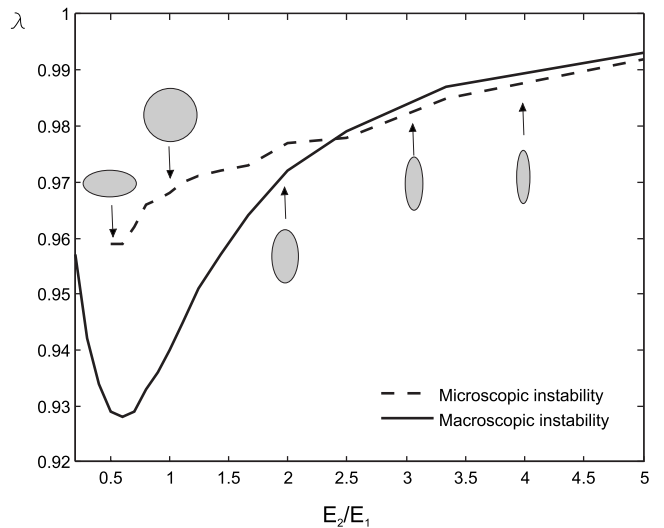

FIG. 19. Applied stretch λ at microscopic and macroscopic instability as function of E_2/E_1.
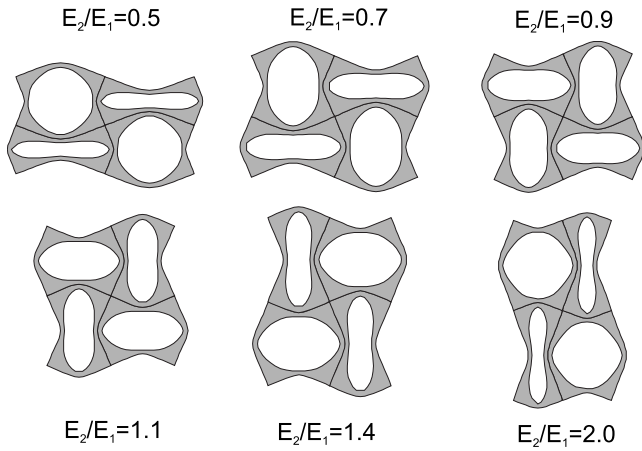
FIG. 20. Eigenmode of the microscopic instability for $E_2/E_1 = [0.5, 0.7, 0.9, 1.1, 1.4, 2]$ as predicted by the Bloch wave analysis.

for E_2/E_1 above 0.5 and below 2. For values of the semiaxes ratio outside this range, macroscopic instability is observed to occur first, resulting in a collapse band perpendicular to the loading direction. Increasing the ratio E_2/E_1 above 0.6, both microscopic and macroscopic instabilities are observed to occur earlier along the loading path. Figure 20 shows the evolution of the eigenmode of the microscopic instability for $E_2/E_1 = [0.5, 0.7, 0.9, 1.11.42]$. For increasing values of $|E_2/E_1 - 1|$ a gradual transition is observed from a pattern of alternating, mutually orthogonal, ellipses to a pattern of alternating ellipses with low and high aspect ratio.

b. Stress-strain behavior. Nominal stress vs applied stretch λ curves for $E_2/E_1 = [0.5, 1, 2]$ are shown in Fig. 21. As predicted by the instability analysis, decreasing the ratio E_2/E_1 results in the instability to occur later along the loading path.

c. Propagation of acoustic waves. The propagation of acoustic waves through infinite periodic solids with elliptical voids characterized by $E_2/E_1 = 0.5$ and 2 are considered. The
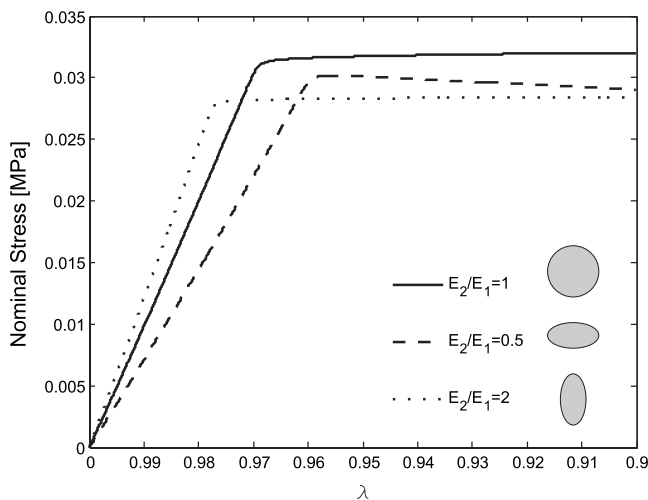

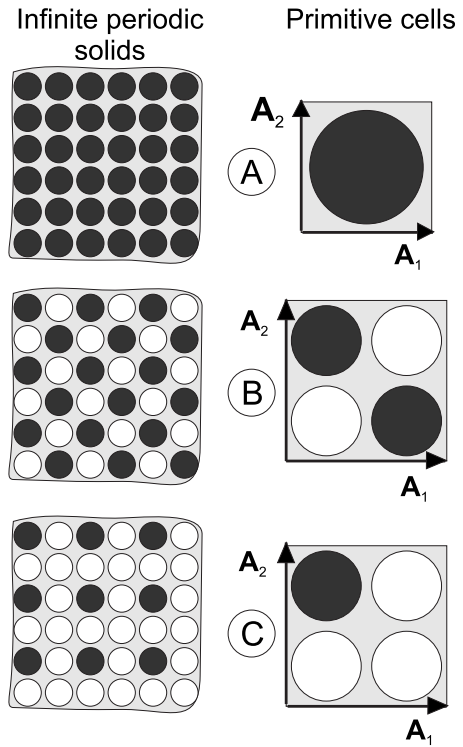FIG. 21. Nominal stress vs applied stretch λ curves for $E_2/E_1 = [0.5, 1, 2]$.

FIG. 22. Infinite square array of circular voids and inclusions.

absence of band gaps both in the undeformed and deformed configuration has been observed in both cases. Moreover a negligible effect of deformation on the phononic band gaps of the solid is found.

5. Effect of inclusions

The effect of inclusions is investigated considering the following three different distributions of inclusions in a neo-Hookean matrix subjected to uniaxial compression as shown in Fig. 22.

(i) solid A: square array of circular inclusions characterized by an initial inclusion volume fraction $f_0 = 0.6$, such that the primitive cell **Y** is defined by the lattice vectors $\mathbf{A}_1 = [R_0\sqrt{\pi/f_0} \ \ 0]$ and $\mathbf{A}_2 = [0 \ \ R_0\sqrt{\pi/f_0}]$;

(ii) solid B: square array of circular inclusions alternating with circular voids, such that the primitive cell **Y** is defined by the lattice vectors $\mathbf{A}_1 = [2R_0\sqrt{\pi/f_0} \ \ 0]$ and $\mathbf{A}_2 = [0 \ \ 2R_0\sqrt{\pi/f_0}]$. The sum of the initial inclusions and void volume fraction is chosen to be $f_0 = 0.6$;

(iii) solid C: square array of circular inclusions alternating with circular voids, such that the primitive cell **Y** is defined by the lattice vectors $\mathbf{A}_1 = [2R_0\sqrt{\pi/f_0} \ \ 0]$ and $\mathbf{A}_2 = [0 \ \ 2R_0\sqrt{\pi/f_0}]$. The sum of the initial inclusions and void volume fraction is chosen to be $f_0 = 0.6$.

a. Analysis of instability. Both microscopic and macroscopic instabilities are investigated for the three infinite periodic solids shown in Fig. 22. The critical values of the applied stretch λ at microscopic instability λ_{micro} and at macroscopic instability λ_{macro} are reported in Table III. Interestingly the introduction of stiff inclusions is found to suppress

TABLE III. Critical stretch λ_{micro} at microscopic instability and λ_{macro} at macroscopic instability.

Geometry	λ_{micro}	λ_{macro}
A	—	0.946
B	—	—
C	—	0.934

the microscopic instability, so that for solids A and C the critical instability has a macroscopic character. Differently for solid B pore closure is detected before macroscopic instability.

b. Stress-strain behavior. Figure 23 shows the stress-stretch behavior for the three infinite periodic structures subjected to uniaxial compression. Solid A where all the inclusions are filled with gold is characterized by greater stiffness, but loss of ellipticity corresponding to localization of deformation occurs much earlier along the loading path than for the other cases.

Solid B, when deformed, is characterized by the emergence of a pattern of alternating circles (the stiff inclusions) and ellipses (the pores). Differently from the case of the square array of circular voids presented earlier, this is not the result of an elastic instability, but the pattern develops gradually with deformation to meet compatibility and accommodate the imposed deformation. In this case the stress-strain behavior is not characterized by a plateau region.

c. Propagation of acoustic waves. The band diagram for solid A in the undeformed configuration is provided in Fig. 24. Since localization of deformation occurs early along the loading path for this periodic structure, a negligible effect of deformation on the phononic band gaps is observed. The stiff inclusions widen the band gaps of the periodic solid. The first complete band gap is observed to occur at a higher normalized frequency for solid A, when compared the case of a square array of circular voids. The evolution of the band
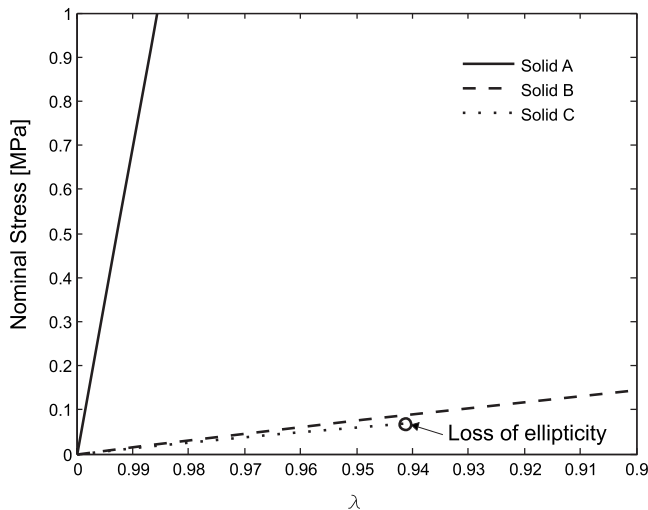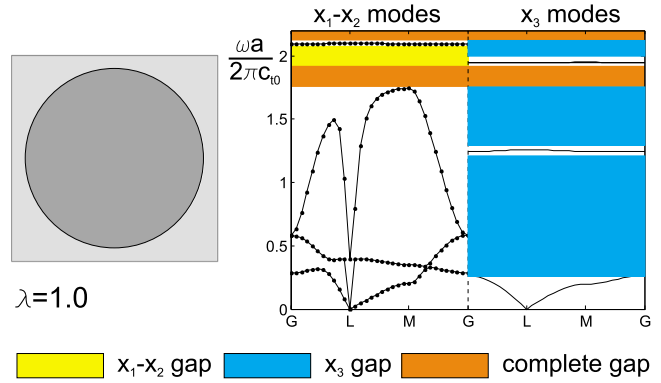

FIG. 24. (Color online) Phononic band-gap structure for solid A in the undeformed configuration. In-plane (labeled x_1-x_2) and out-of-plane (labeled x_3) modes are reported on the left and right part of the plots. The points G, L, and M are defined in Fig. 3.

gaps with deformation or the case of solid B is reported in Fig. 25. The undeformed configuration of the periodic structure possesses five separate out-of-plane x_3 band gaps for $\tilde{\omega}=[0.13-0.88, 0.9-1.22, 1.24-1.61, 1.77-1.83, 1.93-2.04]$ that are only marginally affected by the pattern transformation. The undeformed structure exhibits four separate in-plane x_1-x_2 band gaps for $\tilde{\omega}=[0.26-0.86, 0.88-1.42, 1.64-1.70, 1.90-2.07]$. The width and location of the two lowest-frequency in-plane band gaps are not strongly affected by the deformation. Instead the width of the third and fourth gaps is observed to reduce progressively with increasing deformation and it closes completely for λ equal to 0.9 and 0.85, respectively. Solid B is not characterized by microscopic instability and the deformation develops gradually and monotonically. This behavior is found to affect the
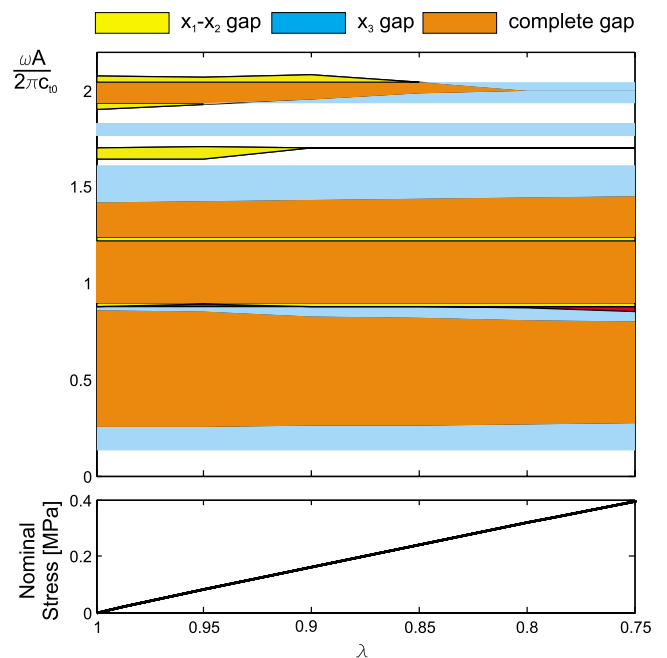

FIG. 25. (Color online) Phononic band gap (top) and nominal stress (bottom) vs applied stretch λ for solid B subjected to uniaxial compression.

FIG. 23. Nominal stress vs applied stretch λ for solids A, B, and C subjected to uniaxial compression.
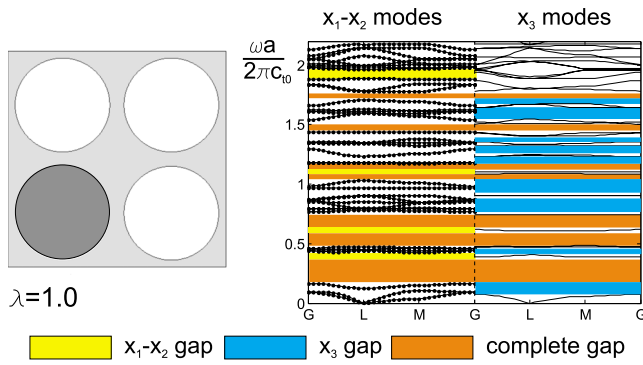
FIG. 26. (Color online) Phononic band-gap structure for solid C in the undeformed configuration. In-plane (labeled x_1-x_2) and out-of-plane (labeled x_3) modes are reported on the left and right part of the plots. The points G, L, and M are defined in Fig. 3.

evolution of the phononic band gaps. Differently from the square array of circular voids, in solid B the in-plane band gaps evolve affinely and monotonically. The third and fourth gaps are observed to close, but their closure occurs at two different levels of deformation, so that there is not a specific level of deformation where the band gaps undergo a transformation.

For solid C, macroscopic instability occurs at an early stage and therefore the effects of deformation on the band structure are negligible. Therefore only the band structure in the undeformed configuration is reported in Fig. 26.

In conclusion, the stiff inclusions are observed to increase the number and width of the phononic band gaps of the structure. On the other hand, the microscopic instability that characterized the square array of circular holes is found to disappear when the inclusions are introduced and in most of the cases a macroscopic instability is observed to occur earlier. This behavior eliminates the possibility of using deformation to suddenly transform the phononic band gaps of the structures.

IV. CONCLUSIONS

The mechanics of deformation of several two-dimensional periodic elastomeric structures have been investigated and the influence of such deformation on phononic band gaps is ascertained. Recently certain periodic porous elastomeric solids have been found to be characterized by a deformation-induced homogeneous pattern transformation.[28,29] In addition it has been shown that the phononic band structure evolves in a monotonic manner during the linear region of the nominal stress-strain behavior when the deformation of the inherent structure pattern is relatively affine. When the periodic pattern transforms to a new pattern upon reaching the critical load, the evolution in the phononic band gap also changes in a nonaffine manner.[30] Recent investigations focusing on tunable phononic band-gap systems have shown that the properties of phononic crystals can be modified by (i) using the piezoelectric effect which altered out-of-plane modes,[38] (ii) through direct physical rotation of elements in a 2D periodic

system of rods hosted in air,[39] and (iii) through direct physical changing of the positioning and dimensions of the periodic geometry.[40,41] However, to our knowledge, the use of deformation to tune and transform the band structure of periodic elastomeric solids has never been considered.

Here, firstly the propagation of acoustic waves through monolithic solids under stress has been investigated. Then the effect of material constitutive law, loading conditions, shape of the voids and presence of inclusions on both the mechanical stability and the wave propagation have been investigated, showing different possibilities for tuning both the pattern transformation and the phononic band gaps.

The effects of a material that stiffens with strain on both stability and phononic band gaps were studied considering a Gent rubber elastic matrix. The material stiffening is found to strongly affect the material response of both the monolithic and the periodically structured hyperelastic solids. The stiffening effect is related to the developing alignment of the macromolecular network[42] and hence induces privileged directions inside the material, so that the deformation has relevant effects on the propagation of acoustic waves. Hence, the phononic band gaps of the periodically structured Gent solid are strongly affected by deformation even in absence of pattern transformation.

Differently, in periodically structured neo-Hookean solids the phononic band gaps are mainly governed by the difference in the initial material properties and the shape of the interface between the different constituent materials. Thus, in absence of pattern transformation, large levels of deformation need to be reached to have relevant effects on the phononic band gaps. Instead, pattern transformation induces a sudden and dramatic change of the interface shape, so that the phononic band gaps are strongly affected.

Loading conditions are found to strongly affect the mechanical behavior of periodically structured hyperelastic structures. In fact, for the structures studied here, mechanical instabilities and resulting pattern transformations are observed only when the solids are subjected to uniaxial or equibiaxial compression.

The shape of the voids is also an important factor. Both the critical eigenmode and the phononic band gaps are found to strongly depend on the initial geometry of the periodically structured solid.

Finally, with the placement of stiff and high-density inclusions on one hand microscopic instability is suppressed, but on the other hand macroscopic instability occurs earlier. This behavior eliminates the possibility of a sudden transformation of the phononic band gaps of the structures at low levels of deformation. However, the phononic band gaps are observed to widen when the stiff and high-density inclusions fill partly or completely the voids.

ACKNOWLEDGMENTS

[1] L. J. Gibson and M. F. Ashby, *Cellular Solids: Structure and Properties* (Cambridge University Press, Cambridge, 1997).

[2] M. S. Kushwaha, P. Halevi, L. Dobrzynski, and B. Djafari-Rouhani, Phys. Rev. Lett. **71**, 2022 (1993).

[3] M. S. Kushwaha and B. Djafari-Rouhani, J. Appl. Phys. **80**, 3191 (1996).

[4] M. S. Kushwaha and B. Djafari-Rouhani, J. Appl. Phys. **88**, 2877 (2000).

[5] M. Kafesaki, M. M. Sigalas, and E. N. Economou, Solid State Commun. **96**, 285 (1995).

[6] J. O. Vasseur, B. Djafari-Rouhani, L. Dobrzynski, M. S. Kushwaha, and P. Halevi, J. Phys.: Condens. Matter **6**, 8759 (1994).

[7] J. O. Vasseur, B. Djafari-Rauhani, L. Dobrzynski, and P. A. Deymier, J. Phys.: Condens. Matter **9**, 7327 (1997).

[8] J. O. Vasseur, P. A. Deymier, A. Khelif, Ph. Lambin, B. Djafari-Rouhani, A. Akjouj, L. Dobrzynski, N. Fettouhi, and J. Zemmouri, Phys. Rev. E **65**, 056608 (2002).

[9] M. Sigalas and E. N. Economou, Solid State Commun. **86**, 141 (1993).

[10] A. Khelif, P. A. Deymier, B. Djafari-Rouhani, J. O. Vasseur, and L. Dobrzynski, J. Appl. Phys. **94**, 1308 (2003).

[11] O. Sigmund and J. S. Jensen, Philos. Trans. R. Soc. London, Ser. A **361**, 1001 (2003).

[12] P. Langlet, A. C. Hladky-Hennion, and J. N. Decarpigny, J. Acoust. Soc. Am. **98**, 2792 (1995).

[13] M. Åberg and P. Gudmundson, J. Acoust. Soc. Am. **102**, 2007 (1997).

[14] C. G. Poulton, A. B. Movchan, R. C. McPhedran, N. A. Nicorovici, and Y. A. Antipov, Proc. R. Soc. London, Ser. A **456**, 2543 (2000).

[15] M. Maldovan and E. L. Thomas, Appl. Phys. Lett. **88**, 251907 (2006).

[16] P. St. Russell, E. Marin, A. Diez, S. Guenneau, and A. B. Movchan, Opt. Express **11**, 2555 (2003).

[17] S. Guenneau, A. Movchan, C. Poulton, and A. Nicolet, Q. J. Mech. Appl. Math. **57**, 407 (2004).

[18] M. Campbell, D. N. Sharp, M. T. Harrison, R. G. Denning, and A. J. Turberfield, Nature (London) **404**, 53 (2000).

[19] S. John, Phys. Rev. Lett. **58**, 2486 (1987).

[20] M. Ulbricht, Polymer **47**, 2217 (2006).

[21] M. Théry, V. Racine, A. Pépin, M. Piel, Y. Chen, J. B. Sibarita, and M. Bornens, Nat. Cell Biol. **7**, 947 (2005).

[22] S. J. Hollister, Nature Mater. **4**, 518 (2005).

[23] M. Geissler and Y. N. Xia, Adv. Mater. (Weinheim, Ger.) **16**, 1249 (2004).

[24] N. Bowden, S. Brittain, A. G. Evans, J. W. Hutchinson, and G. M. Whitesides, Nature (London) **393**, 146 (1998).

[25] D. Y. Khang, H. Q. Jiang, Y. Huang, and J. A. Rogers, Science **311**, 208 (2006).

[26] D. P. Holmes and A. J. Crosby, Adv. Mater. (Weinheim, Ger.) **19**, 3589 (2007).

[27] C. M. Stafford, C. Harrison, K. L. Beers, A. Karim, E. J. Amis, M. R. Vanlandingham, H. C. Kim, W. Volksen, R. D. Miller, and E. E. Simonyi, Nature Mater. **3**, 545 (2004).

[28] T. Mullin, S. Deschanel, K. Bertoldi, and M. C. Boyce, Phys. Rev. Lett. **99**, 084301 (2007).

[29] K. Bertoldi, M. C. Boyce, S. Deschanel, S. M. Prange, and T. Mullin, J. Mech. Phys. Solids **56**, 2642 (2008).

[30] K. Bertoldi and M. C. Boyce, Phys. Rev. B **77**, 052105 (2008).

[31] G. Geymonat, S. Muller, and N. Triantafyllidis, Arch. Ration. Mech. Anal. **122**, 231 (1993).

[32] N. Triantafyllidis, M. D. Nestorovic, and M. W. Schraad, ASME J. Appl. Mech. **73**, 505 (2006).

[33] C. Kittel, *Introduction to Solid State Physics*, seventh ed. (Wiley, New York, Chichester, 1986).

[34] S. Guenneau and A. B. Movchan, Arch. Ration. Mech. Anal. **171**, 129 (2004).

[35] A. N. Gent, Rubber Chem. Technol. **69**, 59 (1996).

[36] M. Danielsson, D. M. Parks, and M. C. Boyce, J. Mech. Phys. Solids **50**, 351 (2002).

[37] J. C. Michel, O. Lopez-Pamies, P. Ponte-Castaneda, and N. Triantafyllidis, J. Mech. Phys. Solids **55**, 900 (2007).

[38] Z. Hou, F. Wu, and Y. Liu, Solid State Commun. **130**, 745 (2004).

[39] C. Goffaux and J. P. Vigneron, Phys. Rev. B **64**, 075118 (2001).

[40] D. Caballero, J. Sanchez-Dehesa, C. Rubio, R. Martinez-Sala, J. V. Sanchez-Perez, F. Meseguer, and J. Llinares, Phys. Rev. E **60**, R6316 (1999).

[41] Y. Yao, Z. Hou, and Y. Liu, Phys. Lett. A **362**, 494 (2007).

[42] M. C. Boyce, Rubber Chem. Technol. **69**, 781 (1996).